Rapid crystallisation of precious metal-mineralised layers in mafic magmatic systems

Luke N. Hepworth[1,2], J. Stephen Daly[3,4], Ralf Gertisser[1], Chris G. Johnson[5], C. Henry Emeleus[6†] & Brian O'Driscoll[2*]

[1]*School of Geography, Geology and the Environment, Keele University, Keele ST5 5BG, UK*
[2]*Department of Earth and Environmental Sciences, University of Manchester, Oxford Road, Manchester M13 9PL, UK*
[3]*UCD School of Earth Sciences, University College Dublin, Belfield, Dublin 4, Ireland*
[4]*Irish Centre for Research in Applied Geosciences, Belfield, Dublin 4, Ireland*
[5]*Department of Mathematics, University of Manchester, Oxford Road, Manchester M13 9PL, UK*
[6]*Department of Earth Sciences, Durham University, South Road, Durham DH1 3LE, UK*

[*]Corresponding author: brian.odriscoll@manchester.ac.uk
[†]Deceased

The solidified remnants of mafic magmatic systems host the greatest concentrations of platinum-group metals in the Earth's crust. Our understanding of precious metal mineralisation in these intrusive bodies is underpinned by a traditional view of magma chamber processes and crystal mush solidification. However, considerable uncertainty remains regarding the physical and temporal controls on concentrating these critical metals, despite their importance to modern society. We present high-precision $^{87}Sr/^{86}Sr$ analyses of plagioclase and clinopyroxene from within cm-thick precious metal-enriched layers in the approximately 60 Ma open-system Rum layered intrusion (NW Scotland). Isotopic heterogeneity is present between plagioclase crystals, between clinopyroxene and plagioclase, and within plagioclase crystals, throughout the studied section. Based on these observations, we demonstrate that platinum-group element mineralisation formed by repeated small-volume reactive melt percolation events. The preservation of

Sr isotope heterogeneities at 10-100 µm length-scales implies cooling of the melts that formed the precious metal-rich layers occurred at rates greater than 1 °C per year, and cooling to diffusive closure within 10s-100s of years. Our data highlight the importance of cyclic dissolution-recrystallisation events within the crystal mush and raise the prospect that precious metal-bearing mafic intrusions may form during repeated self-intrusion during cooling and solidification.

A small number of mafic (-ultramafic) intrusive systems, so-called layered intrusions, are responsible for supplying most of society's Pt, Pd and Rh[1-3]. A wealth of field, petrological and geochemical information exists for precious metal deposits in economically significant layered intrusions[2,4,5]. However, uncertainty persists regarding the mechanisms that concentrate precious metals in centimetre-metre thick layers in these intrusions[1,6]. Some models call for ore-forming processes that acted at or close to the putative magma chamber floor[6-8], whereas others invoke relatively low-temperature fluid-rock interactions operating on partly-to-completely solidified assemblages[6,9,10]. This disparity means that there is uncertainty around the temperature and rheology of solidifying crystal mushes during platinum-group element (PGE) concentration.

Improving our understanding of the behaviour of solidifying crystal mushes is therefore central to advancing our knowledge of precious metal enrichment in crustal magmatic systems. Studies of layered intrusions have provided a broad physiochemical framework for understanding how crystal mushes form as cumulates, and during postcumulus modification[11,12]. Melt percolation, reactive flow, melt segregation and mush compaction might all play important roles during solidification[13]. However, critical gaps remain in our understanding of the length- and time-scales over which these processes occur. This is especially important in open magmatic systems where rejuvenation of crystal mushes occurs

following input of relatively hot primitive magma, significantly increasing mush permeability, and leading to reactive through-flow of melt, resulting in a more protracted solidification history[13-15]. Here we investigate PGE-rich cumulates of the classic Rum layered intrusion (NW Scotland; Supplementary Figure 1) to better constrain the drivers and timescales of crystallisation of precious metal-mineralised layers in mafic magmatic systems. Our new microsampled plagioclase and clinopyroxene $^{87}Sr/^{86}Sr$ data unambiguously show isotopic heterogeneities at length-scales of 10-100 μm that can be linked to reactive percolation events within the Rum crystal mush. From these observations, we calculate that individual PGE-rich layers on Rum were emplaced and closed to diffusive equilibration within hundreds of years, a conclusion that lends strong support to the idea that mafic intrusive systems may also exist in 'cold storage' and be rejuvenated by new magma input, similar to their silicic counterparts[13-16].

Magma chamber processes and PGE in the Rum intrusion

The Rum layered intrusion (British Palaeogene Igneous Province) has been a cornerstone for understanding open-system magmatic and sub-volcanic processes for decades[17-19]. Rum is a particularly valuable locality to investigate unresolved questions relating to the timing of PGE mineralisation in layered intrusions. It is well-characterised, superbly exposed and, although not exploited for PGE, it has mineralised layers that are enriched to ppm levels in Pt and Pd[20]. The intrusion was emplaced at ~60 Ma[21] (during opening of the Northeast Atlantic) and is much younger than several layered intrusions that host economically significant PGE-reefs (e.g., the Archaean Stillwater Complex and the Proterozoic Bushveld Complex)[17,22], meaning that the age correction required for Sr isotope data in minerals such as plagioclase and clinopyroxene is negligible[23]. The eastern portion of the Rum intrusion (Eastern Layered Intrusion; ELI) is constructed of 16 macro-rhythmic units, each ~10-100 m thick and

composed of a peridotitic base and a gabbroic top. This arrangement has been interpreted to reflect fractionation of olivine and then plagioclase from successive batches of basaltic or picritic magma[18]. The ~80 m thick Unit 10 package has been held up as an important example of fractional crystallisation of magma for >60 years[18], based on broad trends in mineral chemistry (e.g., olivine Fo contents) and bulk rock $^{87}Sr/^{86}Sr$ compositions (Supplementary Figure 1)[24]. It is sub-divided into four sections as follows: the lower peridotite (~40 m), upper peridotite (~20 m), troctolite (~5 m) and olivine gabbro (~15 m)[18,24].

More recently, it has been suggested that at least 20-30% of the Unit 10 peridotite formed by late-stage addition of aphyric (picritic) and olivine-phyric magmas in small-volume intrusions[25]. In particular, the lower peridotite contains numerous 10-50 cm thick texturally-distinct peridotite layers that exhibit intrusive relationships with the peridotite above and below. Hundreds of millimetric Cr-spinel seams have been documented throughout the lower peridotite[25] (contextual petrological detail for these is provided in Extended Data Figs. 1-3). These Cr-spinel seams are mainly several mm-cm thick and contain base-metal sulfides (e.g., pentlandite, pyrrhotite and chalcopyrite) and platinum-group minerals (e.g., sulfides, arsenides and tellurides). Cr-spinel seams are stratiform, but not stratabound; they are mainly confined to discrete layer boundaries (defined by olivine grainsize changes) but may locally cut up or down into host peridotites (see ref. 24 for further detail). Some Cr-spinel seams bifurcate. A key observation is that intercumulus plagioclase within 1-2 cm on either side of Cr-spinel seams is ubiquitously compositionally zoned (e.g., Extended Data Fig. 2). Zoning can be normal, reverse or oscillatory in nature, but more complex compositional zoning is also typical. Importantly, zoning of intercumulus plagioclase in the Unit 10 peridotites away from Cr-spinel seams is much less common or absent[25]. In the upper peridotite, Cr-spinel seams are absent[25]. The upper peridotite predates

the lower peridotite and its ubiquitous ~1 cm-sized diopside oikocrysts may reflect a metasomatic overprint as a result of upward-migrating melts[25-27]. At the top of the upper peridotite, a c. 20 cm thick pegmatite body occurs at the boundary with the overlying troctolite.

Target samples and intracrystalline Sr isotope variation

Intercumulus crystals form from the interstitial melt in the crystal mush, so they record evidence of melt-rock interaction after the primary accumulation of the cumulus crystal framework. In order to investigate the intercumulus minerals close to the Cr-spinel seams, three such seams (U10A, U10B and U10C, documented further in ref 25) were sampled from a ~3 m interval in the middle of the lower peridotite (Supplementary Figure 1). One of these seams (U10B) occurs along the contact with an intrusive peridotite, but the other two lack this association. Major element chemistry and compositional maps were collected on these samples by electron microprobe (see Methods and Extended Data Figs. 4,5). Zoned intercumulus plagioclase crystals were then selected from the three seams for Sr isotopic analysis (e.g., Fig. 1a). A clinopyroxene from sample U10B was also analysed. One zoned clinopyroxene oikocryst and a zoned plagioclase were analysed from the upper peridotite (U10O; Fig. 1b), as well as both plagioclase and clinopyroxene from the pegmatite body occurring between the upper peridotite and the troctolite (U10PEG). We also report Sr isotope data for intercumulus plagioclase in a Cr-spinel seam from Unit 8 (U8) of the ELI and from a Western Layered Intrusion peridotite (HAR-1). Sampling of individual intra-crystal zones in plagioclase and clinopyroxene was carried out using a New Wave Micromill and unspiked Sr isotopic analyses were performed by thermal ionisation mass spectrometry (see Methods).

The new $^{87}Sr/^{86}Sr$ data are reported in Table 1 and Figures 1, 2 (see also the Supplementary tables). Anhedral intercumulus plagioclase crystals exhibit highly irregular zoning, including dissolution surfaces. Overall, they range in composition between labradorite and bytownite (An_{61-86}). K_2O and TiO_2 correlate negatively with anorthite content, and plagioclase is ubiquitously more anorthitic where it contains Cr-spinel crystals. Plagioclase Sr concentrations mostly range between 250-500 ppm, and Ba and Rb concentrations are consistently <1 ppm. Clinopyroxene is close to end-member diopside in composition. Electron microprobe element maps reveal that the studied clinopyroxene oikocryst in U10O contains complex, patchy zoning, with a positive correlation observed between Cr_2O_3 and Al_2O_3.

Most of the analysed crystals reveal inter- and intracrystalline isotopic heterogeneity. The maximum range (with 2σ uncertainties) of $^{87}Sr/^{86}Sr$ is 0.704026 ±17 to 0.704591 ±8 in the Unit 10 plagioclase and 0.703533 ±23 to 0.704517 ±17 in clinopyroxene. Within a single, oscillatory-zoned plagioclase, three discrete zones yielded $^{87}Sr/^{86}Sr$ values of 0.704337 ±20, 0.704095 ±20 and 0.704052 ±11 (Fig. 1a). The complex patchily-zoned clinopyroxene oikocryst yielded a $^{87}Sr/^{86}Sr$ range of 0.703533 ±23 to 0.703894 ±23 (Fig. 1b). Isotopic disequilibrium also occurs within plagioclase, within clinopyroxene, and between both phases in the pegmatite (Fig. 2). The Sr isotopic variations broadly correspond to major element variation in both plagioclase and clinopyroxene. In the case of plagioclase crystals in the Cr-spinel seams, more anorthitic plagioclase, as illustrated by its brighter back-scattered electron intensity, tends to be characterised by more radiogenic $^{87}Sr/^{86}Sr$ values (Fig. 1a). In the clinopyroxene, low Al_2O_3 (and Cr_2O_3) domains within the oikocryst are characterised by less radiogenic $^{87}Sr/^{86}Sr$.

Reactive melt percolation in the Unit 10 crystal mush

The Cr-spinel seams represent sites of highly-localised reactive melt flow in the lower peridotite crystal mush (Fig. 3). This conclusion is based on a combination of the intercumulus nature of the zoned plagioclase, the locally transgressive nature of the seams, and the 10-100 μm Sr isotope heterogeneities. Simultaneous dissolution of olivine and plagioclase during melting will lead to precipitation of spinel (plus anorthite or forsterite) at a temperature of ~1320°C[28]. The coincidence of Cr-spinel with anorthitic plagioclase in the interstitial areas of the seams, and absence of Cr-spinel from areas where the plagioclase is more sodic, suggests that Cr-spinel crystallised *in situ* during a peritectic reaction within the crystal mush. Picrite melts such as those considered to be the parental melts of the Rum intrusion are considered to have liquidus temperatures on the order of ~1350°C[22,29], so there was likely sufficient heat to drive dissolution. Most of the Unit 10 Cr-spinel seams are up to 1 cm thick, and have a framework of ~30-40 vol.% cumulus olivine, so reactive through-flow of melt was facilitated by the implied high porosity. The Unit 10 Cr-spinel seams are therefore best interpreted as high-flux (high melt/rock ratio) percolation zones and the resulting seam dimensions represent minimum thicknesses and lengths of these zones. Along-strike variation of the percolation zones, including thickness variations, discontinuities and narrowing to tears within the crystal mush are all consistent with the field relations (details in Fig. 3).

In a given crystal, the most anorthitic plagioclase zones tend to have more radiogenic Sr, supporting the suggestion that assimilation of feldspathic cumulate with radiogenic $^{87}Sr/^{86}Sr$ drove Cr-spinel crystallisation[22]. This is consistent with the field relations since the Unit 10 troctolite predates the lower peridotite and has $^{87}Sr/^{86}Sr$ up to 0.70642 ±2[24,25]. The Unit 10 troctolite could have acquired its $^{87}Sr/^{86}Sr$ composition by mixing of ~7% Archaean (Lewisian Complex) quartzo-feldspathic gneiss with Rum picrite[24]. Binary mixing calculations suggest that reaction of picrite ($^{87}Sr/^{86}Sr$ = 0.702705, 244 ppm Sr[29]) and

cumulate (e.g., $^{87}Sr/^{86}Sr$ = 0.70578, 282 ppm Sr; Unit 10 troctolite[24]) require the most radiogenic compositions in our new dataset to have sourced >50% of their Sr from the cumulate. The reactive percolation process was thus capable of 'recycling' crustal $^{87}Sr/^{86}Sr$ signatures in the Rum system at the postcumulus stage. Mass balance considerations for Cr and the PGE also require melt through-flow to have occurred. For example, Unit 10 Cr-spinel seams can contain ~100 ppb Pt[25], which is ~25 times the amount of Pt that could have been concentrated from a 1 mm thick layer of picrite melt[20]. The PGE are mainly associated with base-metal sulfides, which we interpret as by-products of the melt-rock reaction process.

Fluid dynamics and timescales of cooling

It is possible to place further constraints on the nature of the percolation zones in which the Cr-spinel seams formed. A critical observation is that many Unit 10 Cr-spinel seams extend laterally along strike for several tens of metres, without significant thickness changes. The primary controls on fluid flow through a dissolvable matrix can be described by the Damköhler number (*Da*), which relates the amount of reaction that occurs to the flow rate, over a characteristic length scale[30,31]:

$$Da = \frac{R_{eff} L}{\rho_{fluid} \phi_0 \omega_0}$$

The equilibration length (L_{eq}) describes how far the melt may advect before equilibrating with the host rock:

$$L_{eq} = \frac{\rho_{fluid} \phi_0 \omega_0}{R_{eff}}$$

R_{eff} is an effective reaction rate constant (in $kgm^{-2}s^{-1}$), L is the characteristic length scale, $\boldsymbol{\rho}_{fluid}$ is the density of the invading melt and $\boldsymbol{\omega}_0$ is the melt flow rate at porosity $\boldsymbol{\phi}_0$. Values of R_{eff} can be calculated using the dissolution experiments of Donaldson[32], and $\boldsymbol{\omega}_0$ using Darcy's law for melt flow through a porous matrix. Assuming a viscosity of 10 PaS for the

invading picrite, the formation of percolation zones extending 50-100 m along strike require *Da* of ~10^4 and L_{eq} of 2-3 mm. These estimates imply very high degrees of reaction relative to melt flux. As well as underlining the requirement for through-flow of melt as outlined above, they highlight the importance of reactive picritic melts to the formation of Cr-spinel seams and associated PGE enrichment. It is plausible that zones of porous reactive melt percolation changed laterally to reaction within a hot tear, and back again, facilitating the formation of the seams over the observed length-scales (Fig. 3). Although it is likely that numerous percolation events are represented by the Unit 10 Cr-spinel seams, not all of them need have formed at different times. The observation that Cr-spinel seams may bifurcate implies that there are probably subsets of seams associated with single injections of picritic magma. Thus, the >100 Unit 10 seams represent a smaller number of intrusive replenishments. However, if branching networks of percolation zones existed, vertical separation of each zone by >10 cm of peridotite would have been required to allow disequilibrium transport, assuming no interchannel porosity.

Allowing for through-flow of reactive picrite, another question concerns the ultimate fate of this melt, as well as the interstitial melt present before reactive percolation. Hepworth et al.[25] reported the presence of vertically-elongate clinopyroxene crystals in the lower peridotite resembling fluid escape structures. The single clinopyroxene oikocryst analysed from the upper peridotite has less radiogenic Sr than any of the plagioclase analysed in this study, despite the bulk rock upper peridotite compositions being significantly more radiogenic than the lower peridotite bulk rocks[24]. This is consistent with the clinopyroxene oikocrysts of the upper peridotite pseudomorphing melts that escaped from the underlying cumulate pile, following emplacement of the lower peridotite. The pegmatite body at the top of the upper peridotite likely represents isotopically-distinct melts that ponded and solidified beneath the overlying relatively impermeable cap represented by the Unit 10 troctolite.

The preservation of intracrystalline Sr heterogeneity has implications for the timescales of cooling of the Unit 10 peridotite. Using experimentally-derived diffusion coefficients for Sr in plagioclase and diopside[33,34], it is possible to calculate diffusive equilibration times for Sr in these phases. Diffusion of Sr is faster in diopside (Fig. 4a), but the heterogeneities we observe in the oikocryst are on the order of mm apart (Fig. 1b). The Sr variations in plagioclase, on the order of 10-100 μm apart, point to the shortest timescales for cooling in the Rum intrusion. Following Reddy et al.[35] and subsequently Tepley and Davidson[23], diffusivity can be calculated as a function of cooling rate. In Figure 4b, *a* is the length-scale over which diffusion of Sr in labradorite can occur and is plotted against time for cooling rates of 1°C, 0.1°C and 0.01°C per year. Three possible starting temperatures are considered, 1100°C, 1150°C and 1200°C. Although the liquidus temperature of the incoming picrite was likely higher initially, assimilation of feldspathic cumulate probably reduced this to temperatures in the range of those used in the calculations. The calculations suggest that in order to achieve Sr heterogeneities over the length-scales observed, cooling rates were likely to have been in excess of 1°C per year, and cooling to below closure temperatures must have occurred within tens to hundreds of years, orders of magnitude faster than suggested by Tepley and Davidson[23].

An important implication of these calculations as well as our observations more generally is that crystal mushes associated with mafic magmatic systems can form by repeated intrusive magma addition, prior to complete solidification. Although our conclusions do not preclude other parts of the Rum intrusion forming more conventionally (e.g., crystal settling, *in situ* crystallisation at magma chamber margins), our findings are incompatible with the traditional view of layered intrusion formation by uninterrupted cooling and solidification of a magma chamber. With respect to precious metal mineralisation elsewhere on Rum, PGE-rich chromitites at unit boundaries previously attributed to reactions on the

magma chamber floor[20,22] represent an important target for future research in light of the data presented here.

There is some uncertainty associated with extrapolating the model presented here to precious metal-bearing chromitites in larger, economically-significant layered intrusions such as the Bushveld and Stillwater complexes. However, high resolution (U-Pb in zircon) age determinations from cumulates in both of those intrusions attributed the presence of rocks with younger ages underlying those with older ages to periodic intrusion of magma into the crystal mush[36,37,38], in close proximity to important PGE deposits in both cases. The latter studies have not gone unchallenged[39,40], but when combined with the evidence presented here for rapid crystallisation of mafic crystal mushes by repeated self-intrusion, it is clear the long-held paradigm that all layered intrusions form by solidification from the bottom-up (and/or top-down) requires re-evaluation. Our new data highlight the potential for partly-solidified mafic crystal mush zones existing in 'cold storage' to be rejuvenated by new magma input, as has been increasingly recognised in recent years for silicic magmatic systems[15,16,41].

References

1. Cawthorn, R.G., Barnes, S.J., Ballhaus, C. & Malitch, K.N. Platinum-group element, chromium and vanadium deposits in mafic and ultramafic rocks. *Econ. Geol.* **100th Anniversary Volume**, 215-249 (2005).
2. Naldrett, A.J. Magmatic sulfide deposits; geology, geochemistry and exploration. Berlin, Springer Verlag, Germany (2004).
3. Naldrett, A.J. & Duke, J.M. Platinum metals in magmatic sulfide ores. *Science* **208**, 1417-1424 (1980).
4. Eales, H.V. & Cawthorn, R.G. The Bushveld Complex. In: Cawthorn RG (ed) Layered Intrusions. The Nederlands, Elsevier, Amsterdam, pp 181–230 (1996).

5. Godel, B. Platinum-Group Element Deposits in Layered Intrusions: Recent Advances in the Understanding of the Ore Forming Processes. In: Charlier B, Namur O, Latypov R, Tegner C (eds) Layered Intrusions. Springer Science, Netherlands, pp 379-432 (2015).
6. Mungall, J.E. & Naldrett, A.J. Ore Deposits of the Platinum-Group Elements. *Elements* **4**, 253–258 (2008).
7. Latypov, R., Chistyakova, S., Page, A. & Hornsey, R. Field evidence for the in situ crystallisation of the Merensky Reef. *J. Petrol.* **56**, 2341–2372 (2015).
8. Naldrett, A.J., Gasparrini, E.C., Barnes, S.J., Von Gruenewaldt. G, & Sharpe, M.R. The Upper Critical Zone of the Bushveld Complex and the origin of Merensky-type ores. *Econ. Geol.* **81**, 1105-1117 (1986).
9. Boudreau, A.E. & Mc Callum, I.S. Concentration of platinum-group elements by magmatic fluids in layered intrusions. *Econ. Geol.* **87**, 1830–1848 (1992).
10. Boudreau, A. Fluid fluxing of cumulates: The J-M reef and associated rocks of the Stillwater complex, Montana. *J. Petrol.* **40**, 755–772 (1999).
11. Namur, O. et al. Igneous Layering in Basaltic Magma Chambers. In: Charlier, B., Namur O, Latypov, R., Tegner, C. (eds) Layered Intrusions. Springer Science, Netherlands, pp 75-152 (2015).
12. Holness, M.B., Humphreys, M.C.S., Sides, R., Helz, R.T. & Tegner, C. Toward an understanding of disequilibrium dihedral angles in mafic rocks. *J. Geophys. Res. Solid Earth* **117**, B06207 (2012).
13. Cashman, K.V., Sparks, R.S.J. & Blundy, J.D. Vertically extensive and unstable magmatic systems: A unified view of igneous processes. *Science* **355**, 1280 (2017).
14. Annen, C., Blundy, J.D. & Sparks, R.S.J. The genesis of intermediate and silicic magmas in deep crustal hot zones. *J. Petrol.* **47**, 505–539 (2006).

15. Claiborne, L.L., Miller, C.F., Flanagan, D.M., Clynne, M.A. & Wooden, J.L. Zircon reveals protracted magma storage and recycling beneath Mount St. Helens. *Geology* **38**, 1011–1014 (2010).

16. Cooper, K.M., & Kent, A.J.R. Rapid remobilization of magmatic crystals kept in cold storage. *Nature* **506**, 480–483 (2014).

17. Emeleus, C.H., Cheadle, M.J., Hunter, R.H., Upton, B.G.J. & Wadsworth, W.J. The Rum Layered suite. In: Cawthorn, R.G (ed). *Layered igneous rocks. Developments in petrology*, vol 15, Elsevier Science BV: Amsterdam, 404–440 (1996).

18. Brown, G.M. The layered ultrabasic rocks of Rhum, Inner Hebrides. *Philos. Trans. Roy. Soc. Lon. B* **668**, 1–53 (1956).

19. Bédard, J. H., Sparks, R. S. J., Renner, R., Cheadle, M. J. & Hallworth, M. A. Peridotite sills and metasomatic gabbros in the Eastern Layered Series of the Rhum Complex. *J. Geol. Soc. Lon.* **145**, 207–224 (1988).

20. O'Driscoll, B., Day, J.M.D., Daly, J.S., Walker, R.J. & McDonough, W.F. Rhenium-osmium isotopes and platinum-group elements in the Rum Layered Suite, Scotland: Implications for Cr-spinel seam formation and the composition of the Iceland mantle anomaly. *Earth Planet. Sci. Lett.* **286**, 41-51 (2009).

21. Hamilton, M. A., Pearson, D. G., Thompson, R. N., Kelley, S. P. & Emeleus, C. H. Rapid eruption of Skye lavas inferred from precise U–Pb and Ar–Ar dating of the Rum and Cuillin plutonic complexes. *Nature* **394**, 260–263 (1998).

22. O'Driscoll, B., Emeleus, C.H., Donaldson, C.H. & Daly, J.S. Cr-spinel Seam Petrogenesis in the Rum Layered Suite, NW Scotland: Cumulate Assimilation and in situ Crystallisation in a Deforming Crystal Mush. *J. Petrol.* **51**, 1171–1201 (2010).

23. Tepley, F.J. III. & Davidson, J.P. Mineral-scale Sr-isotope constraints on magma evolution and chamber dynamics in the Rum Layered Intrusion, Scotland. *Contrib. Mineral. Petrol.* **145**, 628–641 (2003).

24. Palacz, Z.A. & Tait, S.R. Isotopic and geochemical investigation of unit 10 from the Eastern Layered Series of the Rhum Intrusion, Northwest Scotland. *Geol. Mag.* **122**, 485–490 (1985).

25. Hepworth, L.N., O'Driscoll, B., Gertisser, R., Daly, J.S. & Emeleus, C.H. Incremental Construction of the Unit 10 Peridotite, Rum Eastern Layered Intrusion, NW Scotland. *J. Petrol.* **58**, 137–166 (2017).

26. Holness, M.B., Hallworth, M.A., Woods, A. & Sides, R.E. Infiltration Metasomatism of Cumulates by Intrusive Magma Replenishment: the Wavy Horizon, Isle of Rum, Scotland. *J. Petrol.* **48**, 563–587 (2007).

27. Leuthold, J., Blundy, J.D., Holness, M.B. & Sides, R. Successive episodes of reactive liquid flow through a layered intrusion (Unit 9, Rum Eastern Layered Intrusion, Scotland). *Contrib. Mineral. Petrol.* **167**, 1021–1038 (2014).

28. Morse, S. A. Basalts and Phase Diagrams. New York: Springer, 493 p (1980).

29. Upton, B.G.J., Scovgaard, A.C., McClurg, J., Kirstein, L., Cheadle, M., Emeleus, C.H., Wadsworth, W.J. & Fallick, A.E. Picritic magmas and the Rum ultramafic complex, Scotland. *Geol. Mag.* **139**, 437–452 (2002).

30. Pec, M., Holtzman, B. K., Zimmerman, M. & Kohlstedt, D. L. Reaction infiltration instabilities in experiments on partially molten mantle rocks. *Geology* **43,** 575–578 (2015).

31. Spiegelman, M., Kelemen, P. B. & Aharonov, E. Causes and consequences of flow organization during melt transport: The reaction infiltration instability in compactible media. *J. Geophys. Res. Solid Earth* **106**, 2061–2077 (2001).

32. Donaldson, C.H. The rates of dissolution of olivine, plagioclase and quartz in a basaltic melt. *Mineral. Mag.* **49**, 683–693 (1985).

33. Giletti, B.J. & Casserly, J.E.D. Strontium diffusion kinetics in plagioclase feldspars. *Geochim. Cosmochim. Acta* **58**, 3785–3793 (1994).

34. Sneeringer, M., Hart, S.R. & Shimizu, N. Strontium and samarium diffusion in diopside. *Geochim. Cosmochim. Acta* **48**, 1589-1608 (1984).

35. Reddy, S.M., Kelley, S.P. & Wheeler, J.A. $^{40}Ar/^{39}Ar$ laser probe study of micas from the Seisa zone, Italian Alps: Implications for metamorphic and deformation histories. *J. Metamorph. Geol.* **14**, 493–508 (1996).

36. Mungall, J. E., Kamo, S. L. & McQuade, S. U–Pb geochronology documents out-of-sequence emplacement of ultramafic layers in the Bushveld Igneous Complex of South Africa. *Nature Comms*. **7**, 13385 (2016).

37. Robb, S.J. & Mungall, J.E. Testing emplacement models for the Rustenburg Layered Suite of the Bushveld Complex with numerical heat flow models and plagioclase geospeedometry. *Earth Planet. Sci. Lett.* **534**, 116084 (2020).

38. Wall, C. J., Scoates, J. S., Weis, D., Friedman, R. M., Amini, M. & Meurer, W. P. The Stillwater Complex: integrating zircon geochronological and geochemical constraints of the age, emplacement history and crystallization of a large, open-system layered intrusion. *J. Petrol.* **59**, 153–190 (2018).

39. Latypov, R., Chistyakova, S. & Kramers, J. Arguments against syn-magmatic sills in the Bushveld Complex. *South African Journal of Geology* **120**, 565–574. (2017).

40. Latypov, R. M. (2019). Comments on "The Stillwater Complex: integrating zircon geochronological and geochemical constraints on the age, emplacement history and crystallization of a large, open-system layered intrusion" by C. Wall et al. (*J. Petrol.* **59,** 153–190, 2018). *J. Petrol.* **60,** 1095–1098 (2019).

41. Miller, C.F., Furbish, D.J., Walker, B.A., Claiborne, L.L., Koteas, C.G., Bleick, H.A. & Miller, J.S. Growth of plutons by incremental emplacement of sheets in a crystal-rich host: Evidence from Miocene intrusions of the Colorado River region, Nevada, USA. *Tectonophysics* **500(1-4)**, 65-77 (2011).

Corresponding Author

Correspondence and requests for materials should be addressed to BOD (brian.odriscoll@manchester.ac.uk)

Acknowledgements

LNH acknowledges funding from a Natural Environmental Research Council (NERC) Studentship (grant number: 1361482) and Keele University. Scottish National Heritage (SNH) is thanked for sampling permission on Rum during 2014 and 2015. Peter Greatbatch and David Wilde (Keele University) are thanked for thin-section preparation, as are Andreas Kronz and Gregor Breedveld for assistance with EMPA analysis at the University of Göttingen. Hanna Horsch is thanked for her assistance generating the QEMSCAN images. Michael Murphy (UCD) is also thanked for technical assistance. Sr isotopic analyses were carried out using equipment at the National Centre for Isotope Geochemistry (NCIG), Dublin, which is a joint venture of University College Dublin, Trinity College Dublin, University College Cork and National University of Ireland Galway, funded mainly by Science Foundation Ireland, including Grant No. 04/BR/ES0007/EC07 awarded to JSD. JSD was also supported in part by Science Foundation Ireland Grant No. 13/RC/2092, which is co-funded under the European Regional Development Fund. James Day is thanked for helpful comments on an earlier version of the manuscript.

Author contributions

BOD conceived the study. BOD, LNH and JSD designed the program of work. LNH carried out fieldwork and EMPA analyses. LNH and JSD carried out the chemistry and mass spectrometry for Sr isotope analysis. BOD and CGJ did the Sr diffusion-related calculations. All authors contributed to interpreting the results. BOD wrote the manuscript. BOD, JSD, LNH, RG and CGJ contributed to editing the final version.

Competing interests

The authors declare no competing interests.

Figure Captions

Figure 1. Examples of intracrystalline $^{87}Sr/^{86}Sr$ variation in Unit 10 plagioclase and clinopyroxene. (a) Back-scattered electron micrograph and corresponding interpretive sketch with $^{87}Sr/^{86}Sr$ data (with 2σ uncertainties) for U10C_16. On (a), the white spots/numbers are EMPA analysis points with corresponding anorthite content. The dashed white outlines delineate the microdrilled pits. For (iii), material was drilled from two pits in the same (interpreted) plagioclase zone. (b) Element map (Al) of clinopyroxene oikocryst (U10O_PX). The microdrilled portions of the oikocryst are outlined in white. For 1 and 4, this comprises two drilled pits each. The $^{87}Sr/^{86}Sr$ data are shown below in the interpretive sketch.

Figure 2. Comparison of new plagioclase and clinopyroxene $^{87}Sr/^{86}Sr$ data with a compilation of published data for the Rum intrusion. Included are the $^{87}Sr/^{86}Sr_{initial}$ range of three Rum picrites (grey field)[29], Unit 10 bulk rock (WR) data[24] and Unit 9 clinopyroxene and plagioclase data[23]. Petrological context for sampled localities in the Unit 10 lower and upper peridotites (LP and UP, respectively) is shown in the schematic logs on the left. Uncertainties on the new $^{87}Sr/^{86}Sr$ data are 2σ, and are typically smaller than symbol sizes. Where different symbols are shown at a given stratigraphic level, this denotes analysis of different crystals.

Figure 3. Schematic cartoon illustrating the reactive percolation model discussed in the text. Top left panel (a) illustrates the entire Unit 10 sequence, (b) is a representative field photograph showing typical distributions of intrusive peridotite (highlighted) in outcrop. The centre panel (c) is based on the field relationships (scale is approximate), and conceptually illustrates formation of Sr isotope heterogeneities ($^{87}Sr/^{86}Sr$ values are indicative only) during the formation of one percolation zone. Note the leading fronts or basal/top contacts of

percolation zones (dark green) locally develop chromitite *sensu stricto*, whereas chain-textured Cr-spinel seams signifying porous reactive flow form around olivine crystals. Reactive percolation zones may locally thin, thicken and bifurcate. The presence of >100 Cr-spinel seams throughout the Unit 10 lower peridotite implies that numerous percolation zones such as those illustrated in panel (c) must have existed. The observation that some Cr-spinel seams bifurcate means that the number of replenishments may be less than the number of Cr-spinel seams, and there is no requirement in our model for 'stratigraphically' higher Cr-spinel seams to postdate those that lie underneath them.

Figure 4. Diffusive equilibration calculations. (a) Characteristic diffusion distance ($\sqrt{Dt}$) as a function of temperature for labradorite, anorthite and clinopyroxene. Over a duration of 1 Ma, estimated as the maximum time-frame for cooling of the Rum intrusion[17,23], plagioclase Sr variation at 10-100 μm would not be preserved over the range of T (°C) shown. (b) Plot of calculated length-scale of diffusion of Sr (*a*) versus time (years) for labradorite. Sr isotope variations exist over length-scales of 10-100 μm (grey shaded field along base of plot), so only curves contained completely within the field can be reconciled with our observations.

Table 1. Sr isotope data for plagioclase and clinopyroxene from the Rum layered intrusion. See text for discussion and description of abbreviations used. See Table S4 for further detail.

Methods

Mineral Chemistry. Plagioclase mineral chemical data were obtained using a JEOL JXA-8900RL electron microprobe at the Department of Geochemistry, Geowissenschaftliches Zentrum der Universität Göttingen (GZG) in 2015. The plagioclase compositions were obtained using an acceleration voltage of 20 kV with a beam current of ~80 nA and a typical beam diameter of 20-25 µm. Plagioclase count times on peak and background for Si, Ca, Al, Na, K were 15 s and 5 s, respectively, for Fe were 30 s and 15 s, for Sr and Ba were 360 s and 180 s, respectively, and for Ti were 300 s and 150 s, respectively. Clinopyroxene compositions were obtained with an acceleration voltage of 15 kV, a beam current of 15 nA, and a typical beam diameter of 15 µm. Clinopyroxene count times on peak and background for Si, Na, K, Ti, Fe, Al, Mg, Ca and Mn were 15 s and 5 s, respectively, and 30 s and 15 s for Cr and Ni, respectively. Element maps of Na and Ca-concentrations were obtained of plagioclase zoning, and for Cr, Mg, Ti and Al-zoning in a clinopyroxene oikocryst from the Unit 10 upper peridotite (see also Hepworth *et al.*[25]). Element maps were obtained using an acceleration voltage of 20 kV, with a beam current of ~60 nA, a beam diameter of 2 µm and a dwell time of 50 ms.

Strontium isotope measurements. Back-scattered electron (BSE) images of zoned intercumulus plagioclase were obtained during mineral chemical analysis of peridotite thick sections (>200 µm) using a JEOL JXA-8900RL electron microprobe at the Department of Geochemistry, Geowissenschaftliches Zentrum der Universität Göttingen, Germany, in 2015. Micro-milling targets were then carefully selected based on criteria such as drill-bit diameter (75–200 µm), and least potential mixing, and maximum possible sample excisable (with plagioclase ~400 ppm Sr). Once samples were selected, they were drilled using a New Wave Micromill at the National Centre for Isotope Geochemistry at University College Dublin,

Ireland, following the methods of Davidson *et al.*[41] and Charlier *et al.*[42]. Mixing between zones was avoided by careful sample selection, and although some blending during drilling may have occurred, it was considered to be minimal based on the internal reproducibility between similar samples. Zones were drilled through a bead of 20 µl of millipure water to produce a slurry, which was then collected into a clean beaker (which itself was weighed prior to use), before a further 10 µl of millipure water was placed onto the sample site to collect any remaining sample. To digest the plagioclase residue, 0.8 ml of HF and 0.2 ml of HNO_3 were added to the beaker containing the sample, which was then sealed and left on a hot plate overnight (>12 hrs). After digestion, the solutions were dried under clean air on a hot plate. After cooling, samples were further digested in closed beakers in 0.3 ml aliquots of first concentrated HNO_3 and later in 0.3 ml of c. 4M HNO_3, in order to break down any fluorides possibly present, drying between successive digestions. Subsequently, 0.3 ml of 1M HNO_3 was added to the sample beakers which were left to cool. Ion chromatography was carried out in disposable columns fashioned from pre-cleaned disposable pipette tips using c. 100 mg of Eichrom© SrSPEC (100-150 µm) resin supported on pre-cleaned Teflon frits. Columns were washed with 0.05M HNO_3–8M HNO_3–0.05M HNO_3–1M HNO_3 immediately prior to use. Following sample addition, 1 ml 1M HNO_3 was eluted and discarded, followed by 8M HNO_3 (to remove Ba). The Sr fraction was stripped from the columns using 2 ml 0.05M HNO_3. 0.05 ml (50 µl) was pipetted from the collected Sr solutions and made up to c. 3% HNO_3, centrifuged at 5000 rpm, and Sr concentrations were determined using a ThermoScientific Neptune Multiple Collector ICPMS, calibrated against standard solutions. This served to estimate the amount of Sr available for thermal ionisation mass spectrometry and also provided an estimate of the $^{87}Sr/^{86}Sr$ ratio. $^{87}Sr/^{86}Sr$ ratios were determined by thermal ionisation mass spectrometry (TIMS) on a ThermoScientific Triton instrument using Sr loads, typically ranging in mass from c. 20 – 100 ng (average = c. 40 ng) for plagioclase

and c. 10 ng for clinopyroxene. Strontium fractions (aliquoted if necessary to optimise the loaded mass) were taken up in 1 µl of 0.05M HNO_3 and loaded onto Re filaments with 1 µl of Ta-activator ($TaCl_5$). An age correction of ~60 Ma[21] is not necessary given analytical uncertainty and Rb concentrations <1 ppm in plagioclase[24]. We assume that this assumption applies to clinopyroxene too, based on concentrations of 100-200 ppb Rb reported by Leuthold *et al.*[43] for clinopyroxenes in the adjacent Unit 9 rocks. The Sr concentrations in the blanks were <0.02 ng, and repeat measurements of reference material NBS SRM 987 using sample loads of 20 ng and 50 ng (see Table S4) yielded a mean $^{87}Sr/^{86}Sr$ value of 0.710277 ±31 (2σ, n=13). This value is indistinguishable from the certified value (0.71034 ±26)[44] and also from more precise values, e.g. 0.710249 ±18 to 0.710269 ±23, reported recently by Schannor et al.[45]. The full dataset including analytical uncertainties and standard analyses can be found in Table S4 of the Supplementary Materials.

Data availability

The data generated during this study are all accessible in the main article and accompanying supplementary data files, and have also been deposited with the National Geoscience Data Centre of the British Geological Survey (doi XXX).

References

42. Davidson, J. P., Tepley, F. J. III & Knesel, K.M. Crystal isotope stratigraphy; A method for constraining magma differentiation pathways. *Eos* **79,** 15 (1998).
43. Charlier, B. L. A., Ginibre, C., Morgan, D., Nowell G. M., Pearson, G., Davidson, J. P. & Ottley, C. J. Methods for the microsampling and analysis of strontium and rubidium isotopes at single crystal scale for petrological and geochronological applications. *Chem. Geol.* **232**, 114–33 (2006).

44. Leuthold, J., Blundy, J. D., Holness, M. B. & Sides, R. Successive episodes of reactive liquid flow through a layered intrusion (Unit 9, Rum Eastern Layered Intrusion, Scotland). *Contrib. Mineral. Petrol.* **167**, 1021–1038 (2014).

45. NIST SRM 987 certificate 2007 (https://www-s.nist.gov/srmors/certificates/987.pdf).

46. Schannor, M., Veksler, I.V., Hecht, L., Harris, C., Romer, R.L. & Manyeruke, T.D. Small-scale Sr and O isotope variations through the UG2 in the eastern Bushveld Complex: The role of crustal fluids. *Chem. Geol.* **485**, 100-112 (2018).

Figure 1

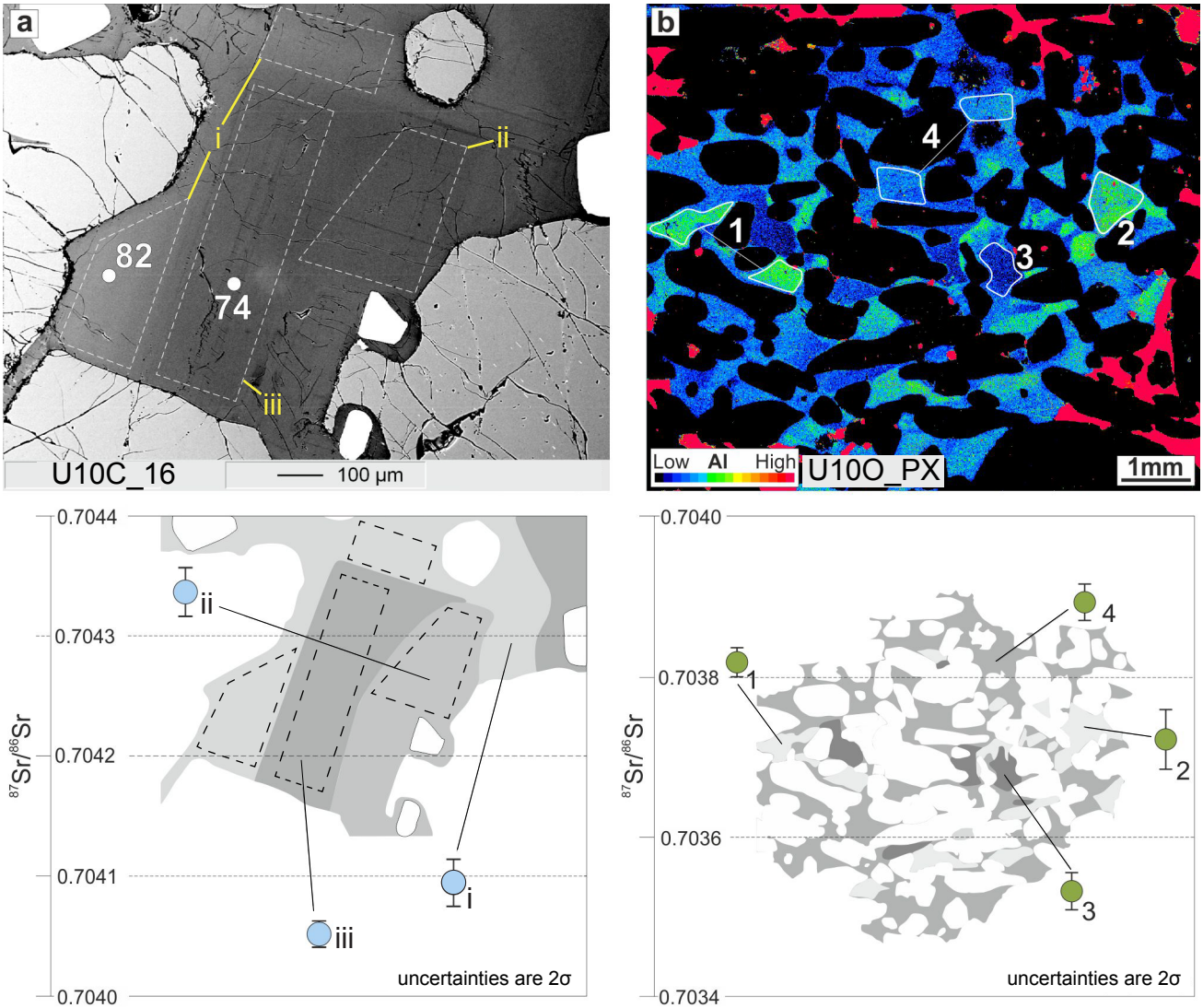
a
i
ii
iii
82
74
U10C_16
100 µm
b
1
2
3
4
Low Al High
U10O_PX
1mm
0.7044
0.7043
0.7042
0.7041
0.7040
87Sr/86Sr
ii
i
iii
uncertainties are 2σ
0.7040
0.7038
0.7036
0.7034
87Sr/86Sr
1
2
3
4
uncertainties are 2σ

Figure 2

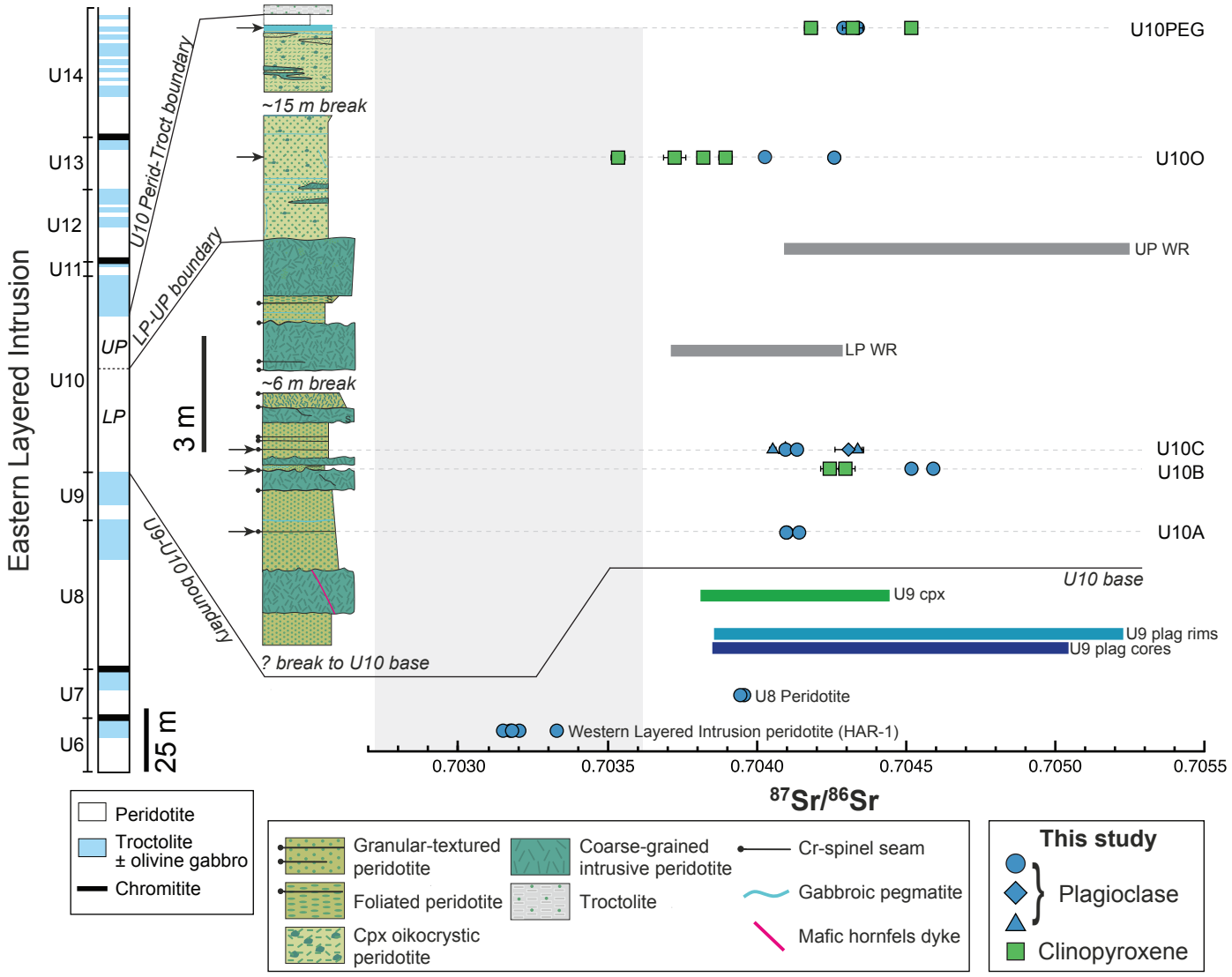
Eastern Layered Intrusion
U14
U13
U12
U11
UP
U10
LP
U9
U8
U7
U6
U10 Perid-Troct boundary
LP-UP boundary
U9-U10 boundary
~15 m break
~6 m break
? break to U10 base
3 m
25 m
U10PEG
U10O
UP WR
LP WR
U10C
U10B
U10A
U10 base
U9 cpx
U9 plag rims
U9 plag cores
U8 Peridotite
Western Layered Intrusion peridotite (HAR-1)
0.7030
0.7035
0.7040
0.7045
0.7050
0.7055
87Sr/86Sr
Peridotite
Troctolite
± olivine gabbro
Chromitite
Granular-textured peridotite
Foliated peridotite
Cpx oikocrystic peridotite
Coarse-grained intrusive peridotite
Troctolite
Cr-spinel seam
Gabbroic pegmatite
Mafic hornfels dyke
This study
Plagioclase
Clinopyroxene

Figure 3

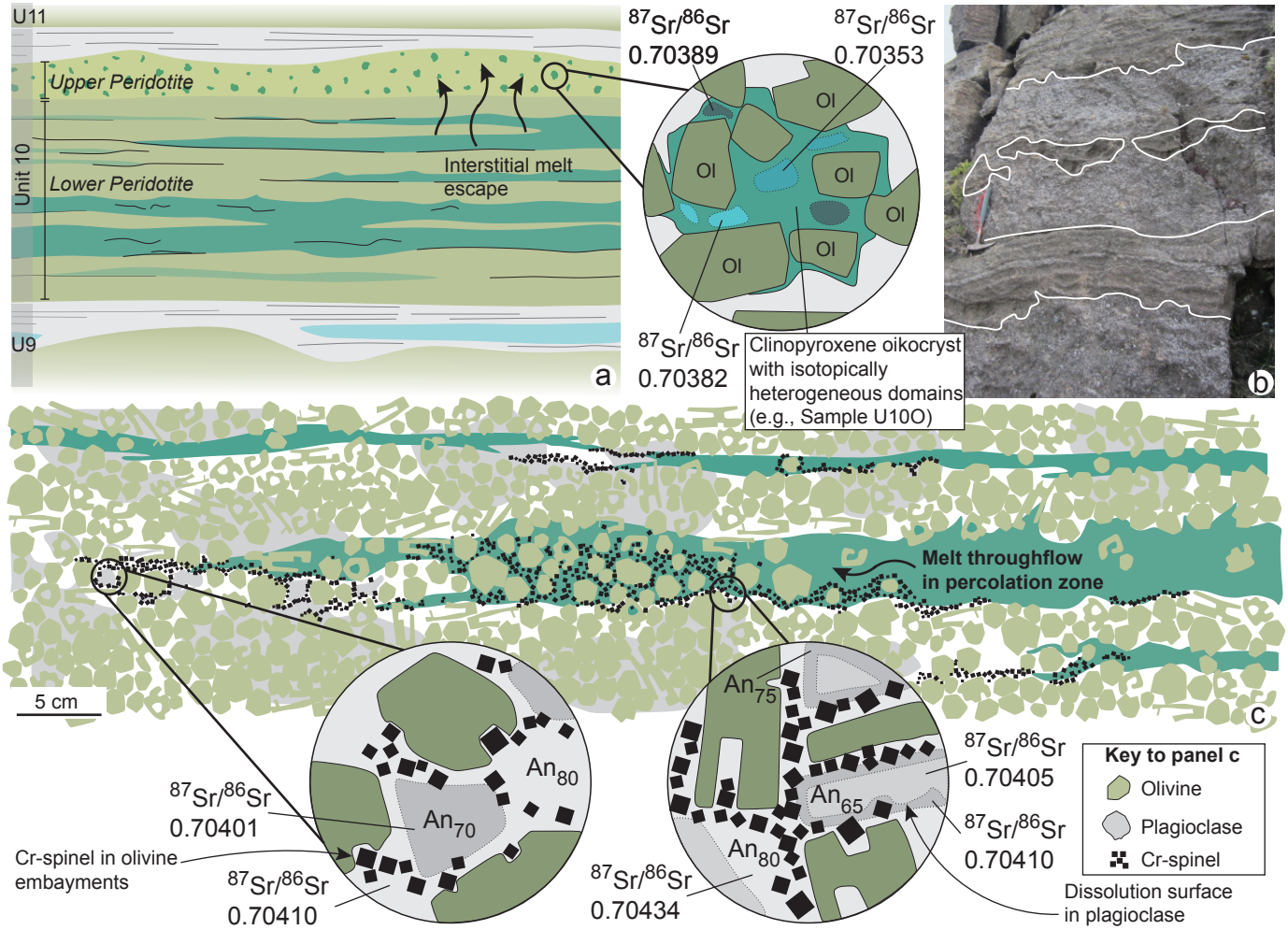
U11
Upper Peridotite
Unit 10
Lower Peridotite
Interstitial melt escape
U9
a
87Sr/86Sr 0.70389
87Sr/86Sr 0.70353
Ol
87Sr/86Sr 0.70382
Clinopyroxene oikocryst with isotopically heterogeneous domains (e.g., Sample U10O)
b
Melt throughflow in percolation zone
5 cm
c
An80
An70
87Sr/86Sr 0.70401
Cr-spinel in olivine embayments
87Sr/86Sr 0.70410
An75
An65
An80
87Sr/86Sr 0.70434
87Sr/86Sr 0.70405
87Sr/86Sr 0.70410
Dissolution surface in plagioclase
Key to panel c
Olivine
Plagioclase
Cr-spinel

Figure 4

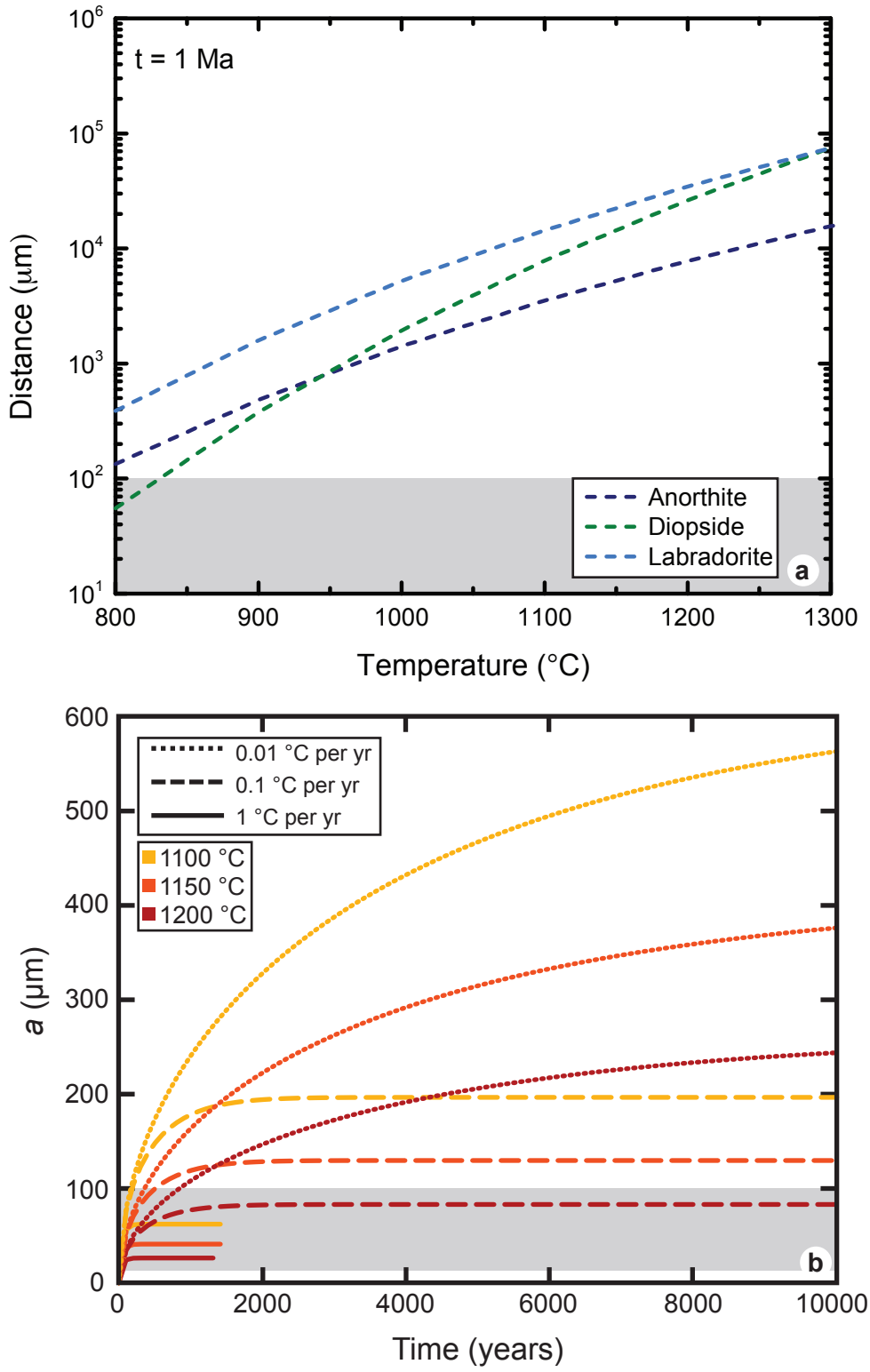
t = 1 Ma
Distance (μm)
Temperature (°C)
Anorthite
Diopside
Labradorite
a
0.01 °C per yr
0.1 °C per yr
1 °C per yr
1100 °C
1150 °C
1200 °C
a (μm)
Time (years)
b

Table 1. Sr isotope data for plagioclase and clinopyroxene from the Rum layered intrusion. See

Plagioclase	$^{87}Sr/^{86}Sr$	2σ (err.)
Unit 10		
U10_PEG_ii	0.704289	0.000015
U10_PEG_i	0.704337	0.000012
U10O_1_ii	0.704026	0.000017
U10O_1_i	0.704259	0.000020
U10C_16_iii	0.704052	0.000011
U10C_16_ii	0.704337	0.000020
U10C_16_i	0.704095	0.000020
U10C_13_i	0.704306	0.000045
U10C_4_ii	0.704095	0.000009
U10C_4_i	0.704134	0.000007
U10B_1_ii	0.704591	0.000008
U10B_1_i	0.704517	0.000009
U10A_12_iii	0.704099	0.000016
U10A_12_ii	0.704098	0.000011
U10A_12_i	0.704141	0.000014
Unit 8		
U8_20_ii	0.703956	0.000009
U8_20_i	0.703943	0.000014
WLI		
HAR-v	0.703202	0.000010
HAR-iv	0.703172	0.000027
HAR-iii	0.703148	0.000014
HAR-ii	0.703178	0.000011
HAR-i	0.703328	0.000016

Clinopyroxene	87Sr/86Sr	2σ (err.)
Unit 10		
U10PEG-PX_i	0.704517	0.000017
U10PEG-PX_ii	0.704321	0.000034
U10PEG-PX_iii	0.704180	0.000021
U10O-PX_1	0.703819	0.000018
U10O-PX_2	0.703723	0.000037
U10O-PX_3	0.703533	0.000023
U10O-PX_4	0.703894	0.000023
U10B-Px_ii	0.704296	0.000032
U10B-Px_i	0.704243	0.000031

text for discussion and description of abbreviations used. See Table S4 for further detail.

Extended Data Figure 1

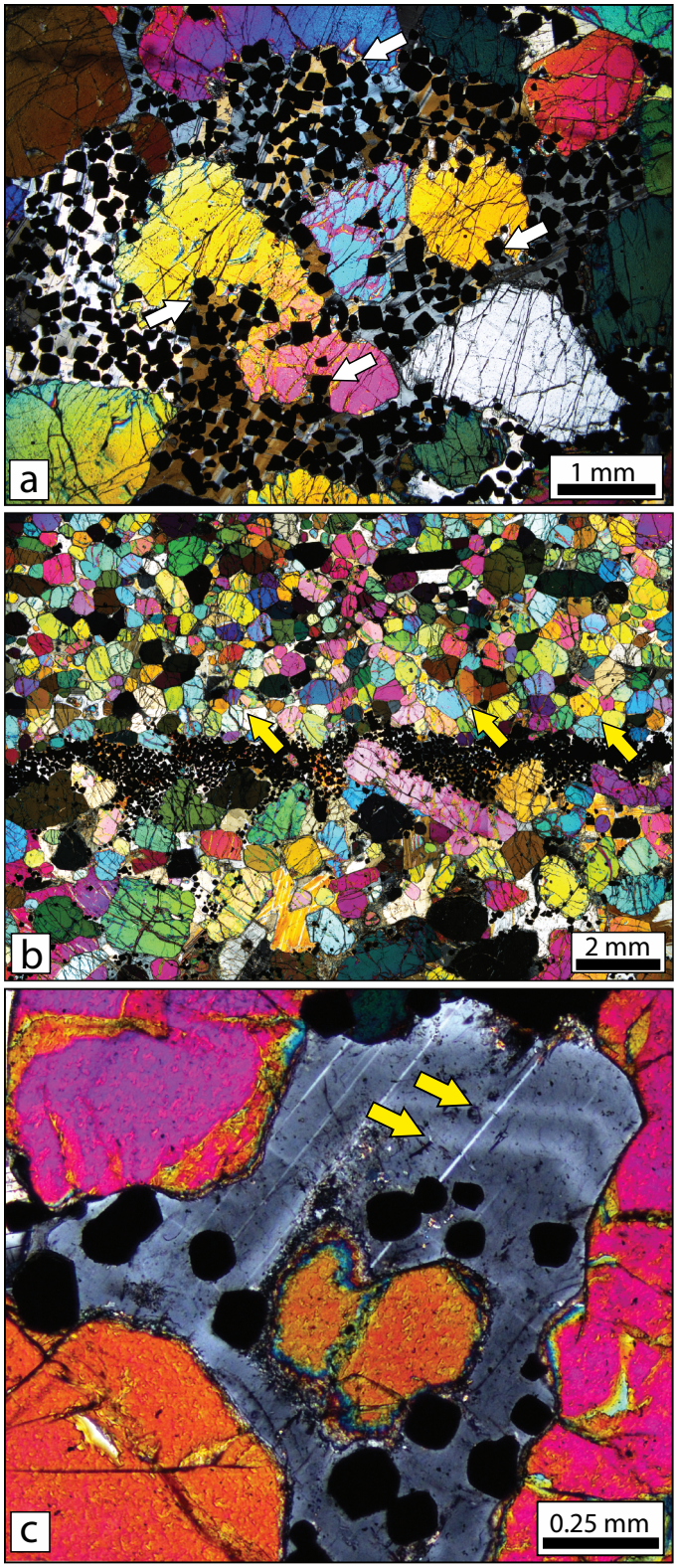

Extended Data Figure 2

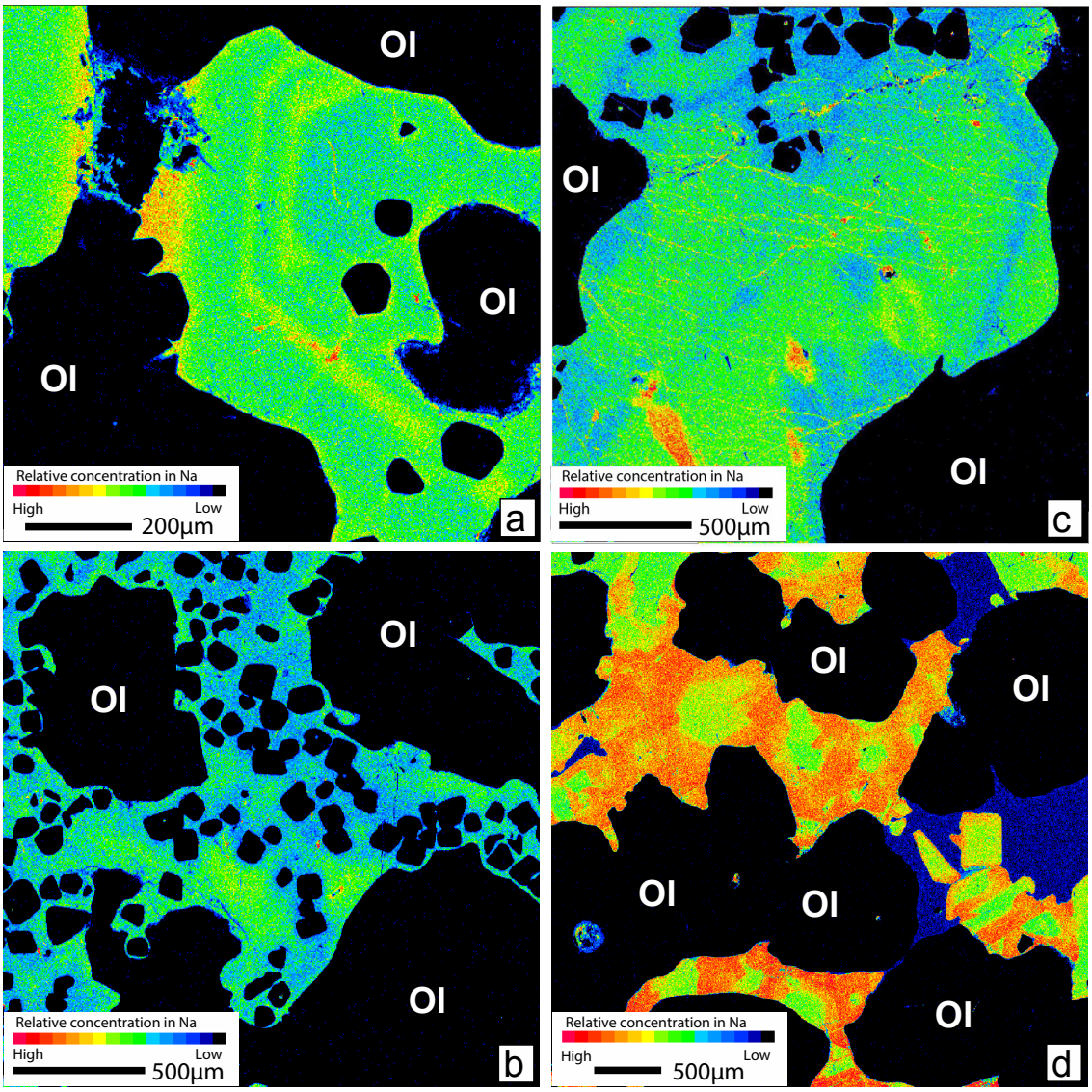

Extended Data Figure 3

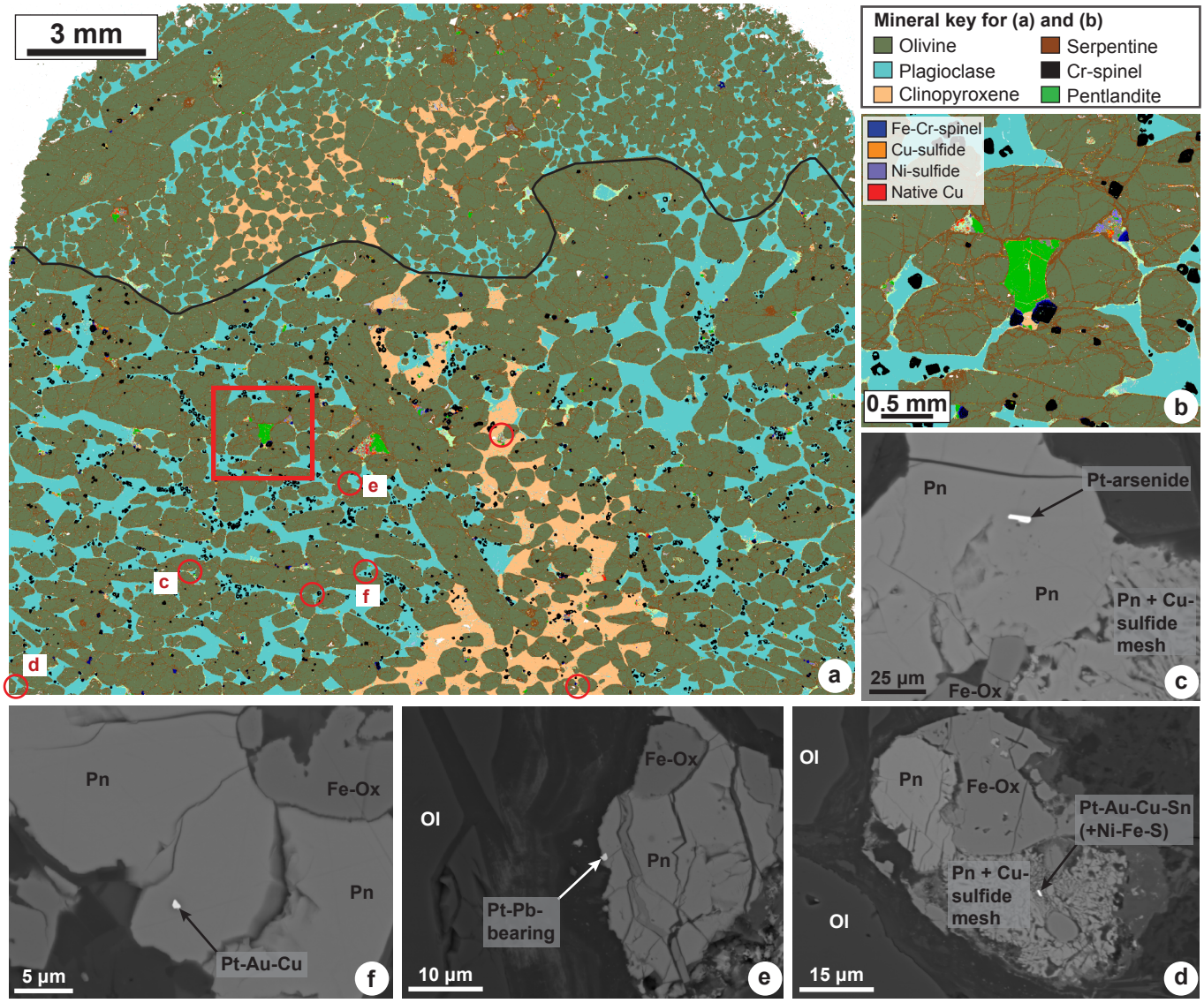

Extended Data Figure 4

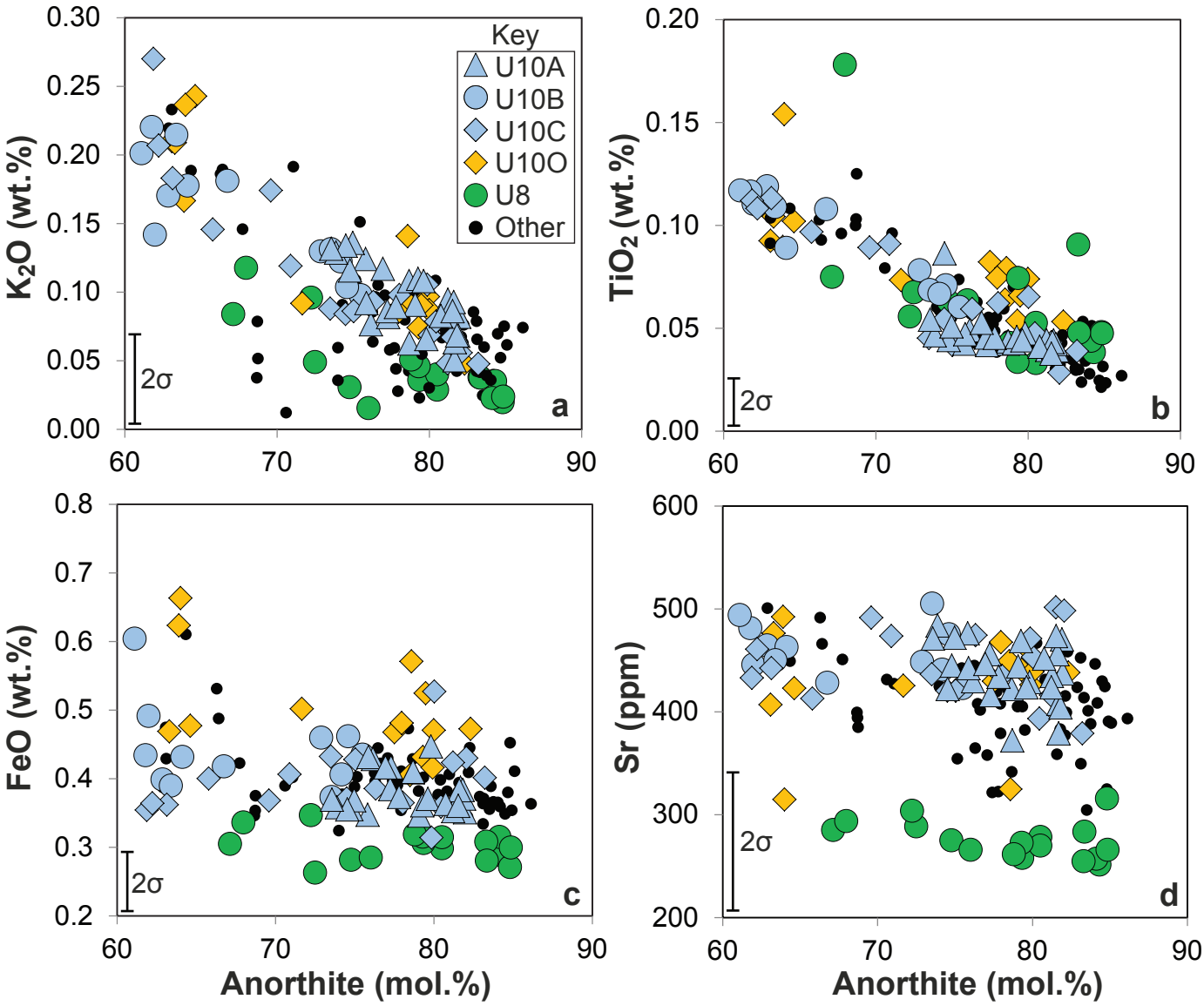

Extended Data Figure 5